Numerical assessment of plastic yielding in extrusion-based 3D concrete printing

Yaxin Tao · **Jiangang Zhou** · **Weijiu Cui** ·
Xinyu Shi · **Geert De Schutter** ·
Kim Van Tittelboom

Abstract Different from conventional mold-cast concrete, extrusion-based 3D printable concrete is deposited layer-by-layer without the support of formwork. Plastic yielding may occur during the 3D printing process, which refers to the non-reversible deformation of the extruded material under load. It is essential to understand and model the plastic yielding of 3D printable concrete in numerical simulations to ensure the high shape stability of 3D-printed elements. To this end, this study explores the influence of process parameters and material properties on the plastic yielding of 3D printable concrete based on computational fluid dynamics (CFD). The material properties were obtained by carrying out flow curve measurements and a Herschel–Bulkley model was adopted. A one-layer element was numerically modeled and validated with the cross-sections of the 3D-printed layer obtained using image analysis. The numerical results agree well with the experiments. After calibrating, the one-layer model was extended to two layers using the user-defined function. The geometrical profile and the plastic-yielded regions in the 3D-printed layers were analyzed as influenced by different process parameters and material properties. Numerical results indicated a high-yielding region in the newly deposited layer, and stresses can be transferred to the underneath layer, resulting in further deformation.

Keywords 3D concrete printing · Numerical simulation · Plastic yielding · Buildability · Computational fluid dynamics

Y. Tao (✉) · G. De Schutter · K. Van Tittelboom
Department of Structural Engineering and Building
Materials, Ghent University, Ghent, Belgium
e-mail: Yaxin.Tao@UGent.be

J. Zhou
Architectural Engineering Institute, Weifang Engineering
Vocational College, Weifang, China

W. Cui
Department of Civil Engineering, Qingdao University
of Technology, Qingdao, China
e-mail: cuiweijiu@163.com

W. Cui
Innovation Institute for Sustainable Maritime Architecture
Research and Technology, Qingdao University
of Technology, Qingdao, China

W. Cui
Intelligent Construction Lab, Qingdao University
of Technology, Qingdao, China

X. Shi
College of Architecture and Urban Planning, Qingdao
University of Technology, Qingdao, China

1 Introduction

Even while earlier historical attempts could be traced, the technology of 3D concrete printing (3DCP) mainly has its roots in the early 2000s when researchers and engineers began exploring in more detail the

potential of additive manufacturing techniques for concrete construction. One of the first known modern 3D-printed concrete structures was a wall element printed in 2003 using the so-called contour crafting approach [1, 2]. Since then, this technology has rapidly evolved, with numerous researchers and companies developing different strategies for printing concrete structures of various sizes and shapes. Several different branches include extrusion-based printing, shotcrete-based printing, powder-based printing, binder jetting, etc. [3, 4]. Among these, the extrusion-based 3DCP is primarily employed, where fresh concrete is extruded at controlled volumes to deposit sequential layers along a pre-defined path [5, 6]. It allows for the construction without the support of formwork, making it possible to create architecturally complex and non-rectilinear structures [7, 8]. However, without gaining high shape stability, also known as high buildability, 3D printable concrete suffers from different types of failures after being extruded without formwork [9, 10].

Two typical failure modes include plastic collapse and elastic buckling, which can lead to instability during placement [11, 12]. Recently, a combination of both failures was also observed [13]. The yield stress of fresh concrete governs the plastic collapse, while the elastic modulus of concrete influences the elastic buckling failure [14]. Therefore, yield stress and elastic modulus play a crucial role in determining the buildability of 3D printable concrete. To evaluate the buildability, different test methods have been proposed. The most commonly used way is the so-called stress growth test where the fresh material is sheared with a vane rotor at a controlled rate and the shear stress as a function of shear strain can be obtained [15]. In addition, the squeeze flow test with a constant force mode was performed to obtain the yield stress of fresh concrete with the consideration of the strength correction factor [16, 17]. Furthermore, the squeeze flow test with an increasing force mode can also be used for the elastic modulus evaluation of the fresh material [18]. In a similar way, the uniaxial unconfined compression test employs cylindrical samples with a higher aspect ratio, as compared to the squeeze flow test. The elastic modulus and the green strength of 3D printable concrete in the fresh state can be obtained [19, 20]. A slow penetration test is also an option, where the evolution of the yield stress can be recorded during hardening [21]. In addition,

a so-called slugs-test has been introduced to assess yield stress at nozzle exit in the case of extrusion-based 3D printing [22]. However, as mentioned, the newly developed 3DCP gives access to freedom of shape that results in complex stress states, even in one printed layer [23]. As a result, most experimental and analytical methods cannot provide comprehensive insights into the stress state of printed layers. Moreover, relying solely on trial-and-error experiments can be laborious and time-intensive.

Numerical simulation has proven to be an efficient approach to understand the behavior of 3D printable concrete in the fresh state [23, 24]. Among different numerical strategies, the finite element method (FEM) has been used to simulate 3DCP by modeling the extrusion process, as well as the behavior of the 3D-printed material and different failure patterns [19, 24]. In this regard, a Grasshopper plug-in for voxel-based numerical simulation of 3DCP has been developed by Vantyghem et al. [13]. In addition, the discrete element method (DEM) was used to simulate the concrete extrusion and deposition processes [25, 26]. A novel simulation model for concrete flow has been introduced, which describes fresh concrete as a collection of particles composed of hard, spherical grains that represent aggregates, surrounded by concentric layers representing mortar or cement paste [25]. In addition, the lattice model with geometric nonlinearity was used to simulate elastic buckling in 3DCP [27]. Computational fluid dynamics (CFD) is an alternative approach to simulate the extrusion process of 3D printable concrete, considering that it has been extensively adopted to model the mixing and pumping stages of fresh concrete [28, 29]. In a recent study, Comminal et al. [30] predicted the cross-sectional shape of a 3D-printed layer through virtual printing simulations in the framework of CFD. Specifically, the authors compared different constitutive laws and discussed the plastic deformation due to self-weight and extrusion pressure. Following that, Spangenberg et al. [31] utilized an elastic-viscous-plastic constitutive model to simulate the flow behavior of 3D-printed layers and predicted the yielded regions of the mortar during printing. Even though, only one representative model was presented showing yielded and unyielded regions. In addition, Mollah et al. [32, 33] investigated the stability of deformable layers during material extrusion additive manufacturing (MEX-AM) by using CFD and predicted the

deformation of 3D printed layers as influenced by the processing parameters (such as printing speeds, extrusion fluxes, layer heights, and nozzle diameters), rheological properties, and the presence of reinforcement. Despite the inspiring outcomes from the studies, the effect of the printing parameters and rheological properties on the formation of local plastic yielded regions during the multiple-layer extrusion process was explored to a limit extent.

In the current study, we focus on the plastic yielding of extruded materials as influenced by process parameters and material properties. First, the model was validated by visualizing and comparing the layer height and width obtained from experimental and numerical results. Furthermore, the geometrical profile of multi-layer elements was evaluated as influenced by different process parameters including the nozzle diameter, the printing speed, and the nozzle height. Finally, the distribution of local plastic yielded regions and the yielded area in multi-layer elements was analyzed.

2 Numerical model

The numerical simulation was carried out with the commercial software package ANSYS Fluent. The single-fluid approach was used to simulate the concrete extrusion process. The pressure–velocity coupling was established by employing the semi-implicit method for pressure-linked equations (SIMPLE). Given the assumption that fresh concrete is an incompressible fluid in an isothermal condition, the fresh concrete was modeled by the continuity and momentum equations [30, 34]:

$$\nabla \cdot \boldsymbol{u} = 0 \tag{1}$$

$$\rho\left(\frac{\partial \boldsymbol{u}}{\partial t} + (\boldsymbol{u} \cdot \nabla)\boldsymbol{u}\right) = -\nabla p + \mu\nabla^2\boldsymbol{u} + \rho\boldsymbol{g} \tag{2}$$

where ρ is the fresh concrete density (kg/m^3), $\boldsymbol{u}$ is the velocity vector (m/s), μ is the viscosity (Pa s), t is the time (s), p is the pressure (Pa), and $\boldsymbol{g}$ is the acceleration due to gravity (m/s^2).

The computational fluid domain of the model comprises the printing nozzle, the planar building surface, the printing path, and the area for material extrusion in Fluent (see Fig. 1). The printing nozzle is modeled as a hollow cylinder with a length of 80 mm, a wall thickness of 2 mm, and varied inner diameters (15, 20 and 25 mm). The planar building surface is 350 mm in length, 80 mm in width, and 5 mm in height. The printing path is created using Rhino/Grasshopper and integrated into the computational domain.

A tetrahedral grid is utilized for the wall of the printing nozzle, while a hexahedral grid is used for the computational fluid domain, with appropriate refinement near the nozzle. Upon importing the mesh model into Fluent, no-slip boundary conditions are applied. Meanwhile, other parts of the computational domain have free boundary conditions, which permit the unrestrained deformation of materials [30]. Moreover, to ensure volume conservation, the extrudate's volume must be identical

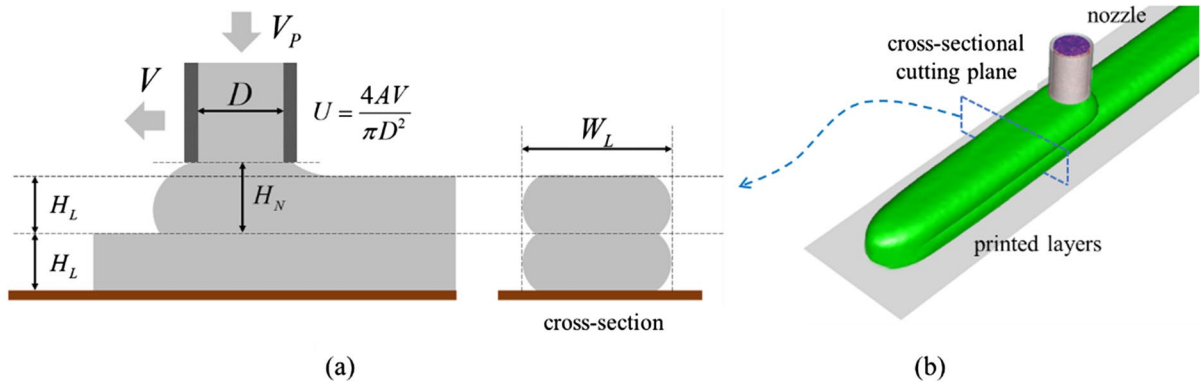**Fig. 1** Computational domain of the numerical model
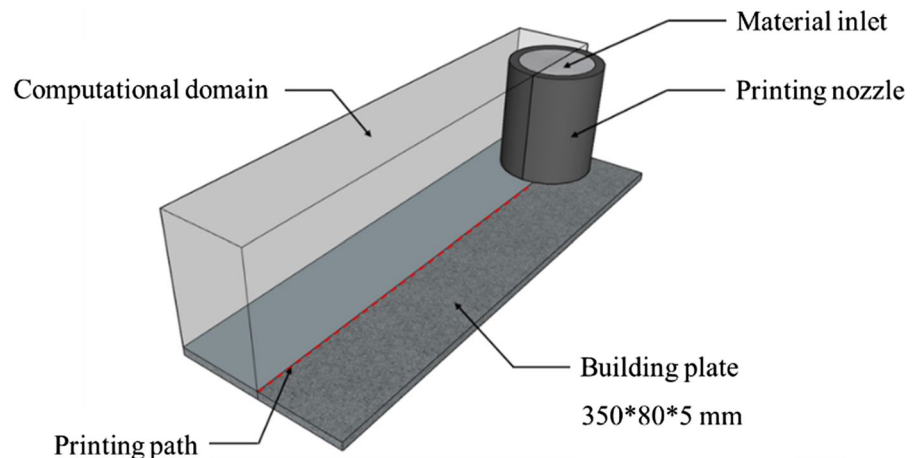
Fig. 2 **a** Schematic views of the extrusion configuration with two layers, and **b** example of cross-sectional plane for image analysis

to the print material's volume, as illustrated in Fig. 2a. The cross-sectional area is determined by the speed ratio $S_R = V/U$, where V represents the printing speed (mm/s) and U represents the material extrusion flux (mm/s), according to the following equation:

$$\frac{1}{4}\pi D^2 U = AV \tag{3}$$

where U is the material extrusion flux (mm/s), D is the nozzle diameter (mm), A is the cross-sectional area of one printed layer (mm^2), and V is the printing speed (mm/s).

Other parameters to be noted include the thickness of one printed layer H_L (mm), the width of one printed layer W_L (mm), and the nozzle height H_N compared to the previous layer (mm).

Custom generation is adopted to describe the fluid movement with the printing nozzle, which is not pre-defined in Fluent. The momentum source terms, which stack on top of each other and move reciprocally during the extrusion of 3D-printed concrete, are loaded using a user-defined function (UDF). This ensures that the source terms of all meshes in the zone are related to the defined coordinates, as well as the interaction between the dynamic meshes of the bottom layer and the second layer. Figure 2b illustrates the effect of the computational model loaded for the two-layer element.

Seven numerical models with varying grid quantities (from 150,000 to 1,000,000, see Fig. 3) were set up individually, while all other material and physical parameter settings were kept the same. This was done to evaluate the impact of mesh refinement on
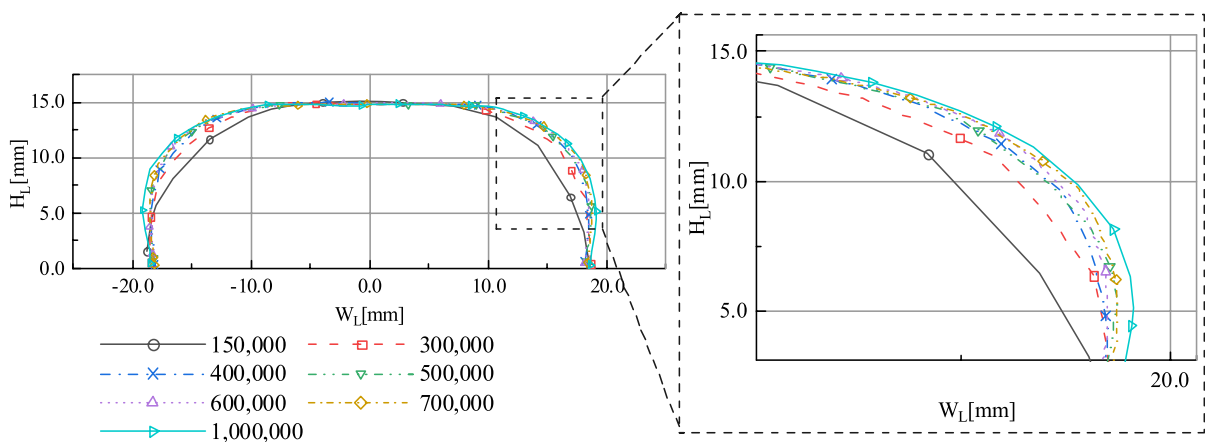

Fig. 3 Cross-sectional profile using different numbers of grids

fluid flow field calculation. The cross-sectional profile obtained from the numerical simulation of single layer 3DCP was compared, as illustrated in Fig. 3. It demonstrates that the grid size directly impacts the shape of the cross-section of the printed layer. When the grid number increases to 400,000 or more, the overall shape of the cross-section remains relatively stable, with a denser data point distribution, resulting in a smoother and more rounded cross-section. The trend of the cross-sectional distribution was similar when the grid number was around 500,000 compared to the larger grid number of about 1,000,000. Hence, a grid number of approximately 500,000 was selected for calculation in this paper, meeting the computational domain requirements while conserving computational resources.

This paper describes the rheological properties of 3D-printed concrete by employing the Herschel–Bulkley model, which will be further discussed in the following section. Different printing speeds, nozzle heights, nozzle diameters, and rheological properties were set in the model to evaluate the influence of printing process parameters and rheological properties on the geometrical profiles and plastic yielding of extruded layers. The established CFD model employed a scalar approach to distinguish the rheological characteristics of two layers [33]. This distinction is crucial for accurately simulating the deposition process, where a fresh layer with a lower yield stress value was deposited onto the bottom printed layer with a yield stress buildup. In the current study, only one mixture with a yield stress value of 405.7 Pa was developed for experimental testing (see Sect. 3.2). To describe the yield stress buildup during 3D printing and to determine the lower and upper boundaries of yield stress values, the highest yield stress value of the bottom layer is determined when the bottom layer remains entirely unyielded in the model, regardless of changes in the second layer. The lowest yield stress value of the second layer is selected when the second layer itself is completely yielded in the model. The other values are linearly interpolated. See more details in Table 1.

3 Experimental program

3.1 Materials and mixture preparation

The current study used Portland cement (52.5 N) and quartz sand with a maximum grain size of 2 mm.

Table 1 Values of the printing parameters and material parameters used in the model

Parameters	Numerical values
Printing speed (mm/s)	10, 20, 30, 40
Nozzle height (mm)	5, 10, 15, 20
Nozzle diameter (mm)	15, 20, 25
Yield stress of bottom layer (Pa)	405.7, 604, 803, 1002, 1201, 1400
Yield stress of second layer (Pa)	190, 243.75, 297.5, 351.25, 405.7
Consistency index	74.07
Power index	0.81

Hydroxypropyl methyl cellulose ether with an amount of 0.15% by the mass of cement and polycarboxylic acid with an amount of 0.1% by the mass of cement was used as the viscosity modifying admixture and the water-reducing admixture, respectively. The solid content of the water-reducing admixture is around 20%. The water-to-cement ratio is 0.35 and the sand-to-binder ratio is 1. The mixture was prepared with the following procedure. First, quartz sand and cement were mixed for 60 s. After that, water with the dissolved water-reducing admixture was added and mixed for 120 s. After scraping and resting for 60 s, the viscosity-modifying admixture was added and continually mixed for 240 s. The rotational speed was controlled constantly at 60 rpm.

3.2 Rheological measurements

The eBT-V rheometer (Schleibinger) equipped with coaxial cylinders was used, where the inner cylinder measures a speed range of 0–40 rpm. The height and diameter of the blade vane rotor were 103 mm and 80 mm, respectively. The capacity of the container was 15 L and the inner diameter was 244 mm (without considering anti-slip bars). The flow curve measurement consisted of two stages. The first stage was the pre-shearing stage (35 rpm for 30 s) to reach a reference state of the material. After pre-shearing, six steps were carried out, with the maximum speed set to 35 rpm and the minimum speed set to 2 rpm. At each testing step, the rotational speed decreased by an equal amount, with a measurement interval of 5 s. Only data points from the last 3.5 s of each interval were collected as speed and torque can fluctuate during the speed change transition period (usually the

first 1.5 s of 5 s). Approximately 50 stable data points were collected for each stage. The Herschel–Bulkley relation will be applied, as expressed:

$$\tau = \tau_0 + k\dot{\gamma}^n \tag{4}$$

where τ denotes the shear stress, τ_0 is the yield stress, $\dot{\gamma}$ is the shear rate, k is the consistency index, and n is the power index.

The flow curve measurements were carried out twice for verification.. The values for the yield stress, the consistency index, and the power index are 405.7, 74.07, and 0.81, respectively. The time-dependent behavior is crucial for 3DCP. In the current study, the time-dependent behavior is considered by assigning different yield stress values to the first and the second layer. More details can be found in Sect. 4.3.1.

3.3 3D printing tests

A gantry type 3D printer was used, which consists of two main components: the printer system and the accessory part (see Fig. 4). The printer system contains the print head, stepping device, and PLC control system, while the accessory part includes the overall frame, printing platform, and other associated elements. The PLC control system governs the overall device stepping and can automatically slice the printing model and optimize the path.

The single-axis stepping speed ranges between 0 and 50 mm/s, and the servo motor's accuracy accounts to 0.01 mm, enabling accurate three-axis linkage. The printer was equipped with a print head compatible with the printing material's largest particle size of 2 mm. The nozzle diameter was 20 mm for the 3D printing tests. In addition, different nozzle heights (10 and 20 mm) and printing speeds (10, 20, 30, and 40 mm) were set to validate the model. Four cross-sections were measured for each series.

3.4 Image analysis

Image analysis was employed to analyze the geometry of layer cross-sections. Initially, the filming device (Andor CCD camera) matrix was calibrated, followed by contour detection utilizing a custom image
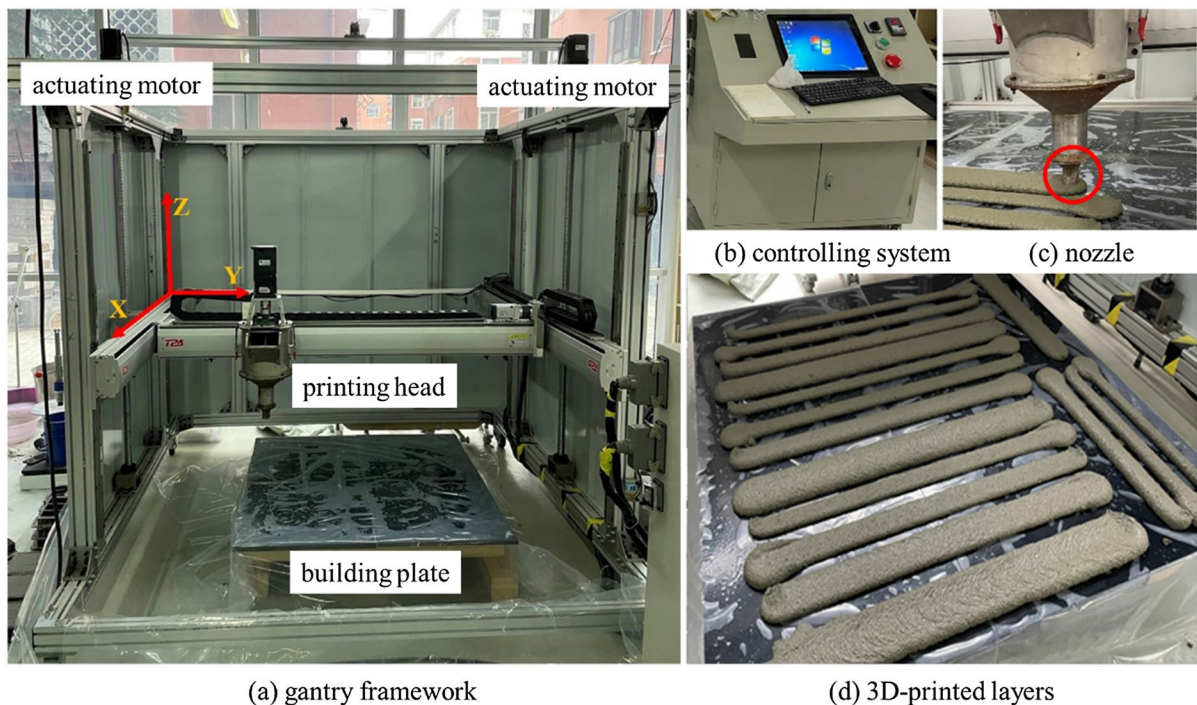

(a) gantry framework

(b) controlling system   (c) nozzle

(d) 3D-printed layers

Fig. 4 3D concrete printing system, including **a** gantry framework, **b** controlling system, **c** printing nozzle indicated in the red circle, and **d** 3D-printed layers

processing script based on spatial filtering and image binarization. The data were calibrated to obtain the coordinates of each corner point in the image. This was achieved by capturing images of the calibration matrix board from different angles using the filming equipment and simulating the image information acquisition conditions and filming environment using the calibration tool library in MATLAB. To further binarize the image, the next step involved converting the grayscale image into a binary image. This is achieved by assigning a value of 1 (white) to all pixels in the input image that have a brightness greater than a specified value (i.e. a threshold value) while assigning a value of 0 (black) to all other pixels. The range of values specified is related to the potential signal level of the image. For example, a value of 0.5 corresponds to a medium intensity value between the minimum and maximum values of the image. After obtaining the binary image, the outline is traced by recognizing non-zero pixels as objects and zero-valued pixels as the background. A specific starting point on the object's boundary is identified, along with the initial search direction for the next object pixel. The row and column coordinates of the pixels along the object's boundary are then saved, creating a smoother cross-sectional profile with more uniformly distributed data points. The height and the width of the layer are then obtained at the central-axis position, i.e. in the middle of the sample.

4 Results and discussion

4.1 Model validation

A visual comparison of layer height and width between numerical and experimental results is shown in Fig. 5, revealing that the model calculation results agree well with the experimental results for different printing speeds. It should be noted that the fluid extrusion flux U was adapted based on the actual cross-section area considering the flow fluctuation in practical printings. This is because the process parameters, as well as the material properties such as cohesion, directly impact the geometrical profile of the extruded layer. A printing speed that is too fast or too slow can result in underfilling or overfilling of the material, as well as fracture of the material in the fresh state [35, 36].

Note that the simulation outcomes may not align with experimental results optimally in extreme cases, such as Case 1 and Case 8 in Fig. 6. In the numerical model, it assumes the fresh concrete as an ideal gravity flow, while in a practical situation, compression can also be caused, as well as the friction at the printing nozzle, especially when admixtures such as cellulose ether are added to 3D printed concrete. There is a likelihood of drag effects occurring because of the cohesive nature of fresh concrete. As a result, the surface of 3D printed concrete tended to be flatter in experiments than the simulated one (see Case 1) when a low printing speed was adopted. Conversely, employing high printing speeds (e.g. 40 mm/s) and substantial nozzle heights (e.g. 20 mm) resulted in a practical printed layer width that is narrower than the simulated counterpart, attributable to the influence of drag forces (see Case 8).

In Fig. 7, a quantitative comparison of the layer height and width between numerical and experimental results with respect to the speed ratio is presented. It shows that as the speed ratio increased, the layer height decreased slightly, while the layer width largely decreased. This follows the actual 3D printing cases where the height of one single layer is mainly controlled by the nozzle height [37, 38]. The results demonstrate that the experimental results correspond to the numerical simulation results, thereby confirming the effectiveness of utilizing the Herschel Bulkley constitutive law to characterize the fresh material.

4.2 Geometrical profile evaluation

4.2.1 Influence of nozzle diameter

The diameter of the printing nozzle can significantly impact the width of the printed layer, therefore, altering the nozzle diameter mainly affects the interlayer bonding state by modifying the contact area between the layers and the flatness of the layer surface [39, 40]. Figure 8a shows that changing only the diameter of the printing nozzle leads to a significant reduction in layer thickness when the nozzle with a smaller diameter is used, as the fluid extrusion flux remains constant ($U = 32.93$ mm/s). Each layer has a concave shape during printing, leading to more significant transverse deformation and more severe geometric defects. Furthermore, the increased local flow raises the likelihood of plastic damage to the printed layer.
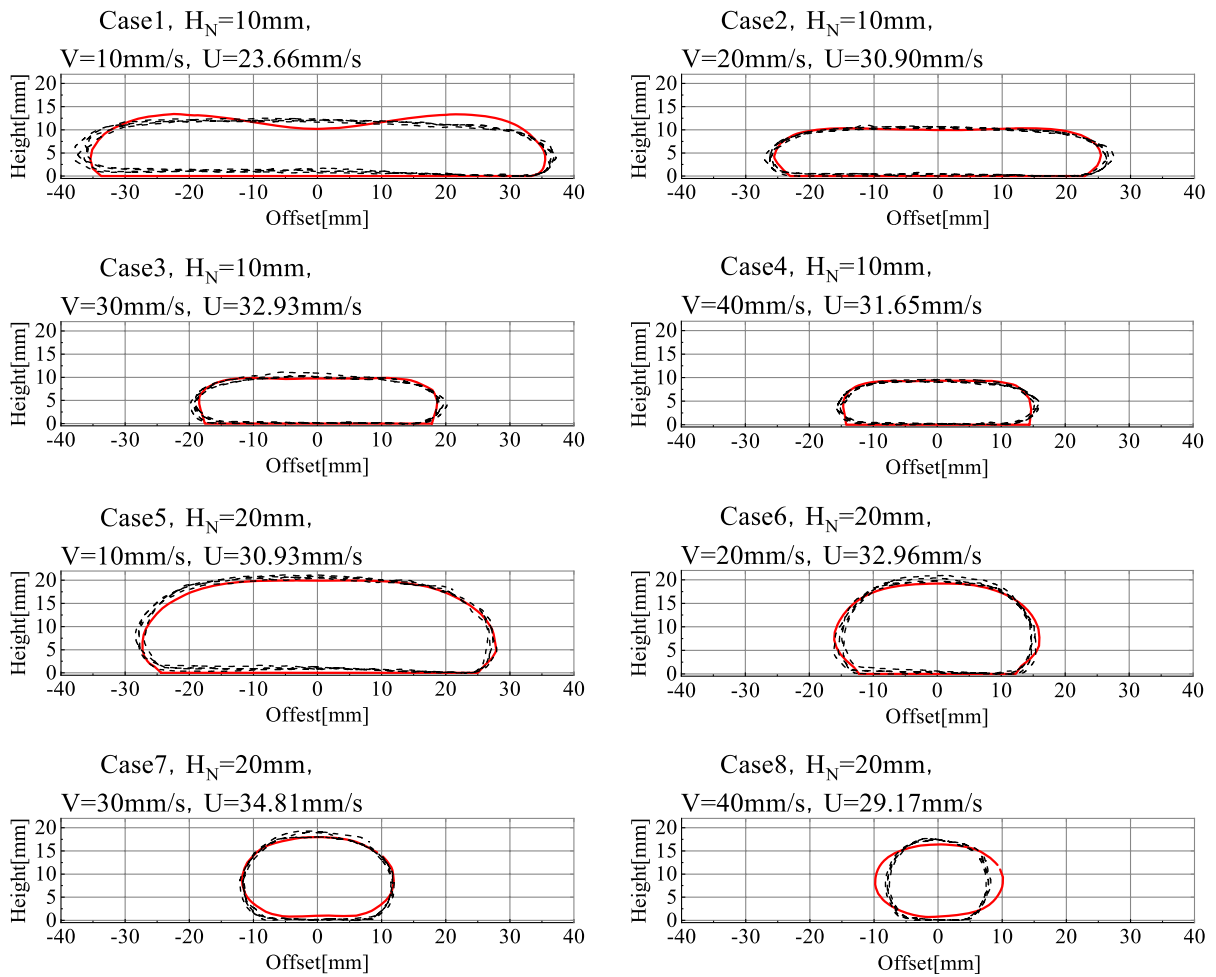
Case1, H$_N$=10mm, V=10mm/s, U=23.66mm/s

Case2, H$_N$=10mm, V=20mm/s, U=30.90mm/s

Case3, H$_N$=10mm, V=30mm/s, U=32.93mm/s

Case4, H$_N$=10mm, V=40mm/s, U=31.65mm/s

Case5, H$_N$=20mm, V=10mm/s, U=30.93mm/s

Case6, H$_N$=20mm, V=20mm/s, U=32.96mm/s

Case7, H$_N$=20mm, V=30mm/s, U=34.81mm/s

Case8, H$_N$=20mm, V=40mm/s, U=29.17mm/s

Fig. 5 Comparison between numerical simulation and experimental results, where red lines indicate numerical results and dashed lines indicate experimental results

Fig. 6 Dragging effect during 3D printing for **a** Case 1, and **b** Case 8

(a)

(b)

Figure 8b illustrates the situation where the fluid extrusion flux is adjusted proportionately to the printing nozzle diameter to maintain the cross-sectional shape of the printed layer. As the diameter increases, the printed layer tends towards a rectangular shape, resulting in a larger contact area. In addition, the increased diameter expands the range of stresses acting on the printing nozzle, reducing the occurrence of stress concentration and minimizing overall deformation, which will be

further discussed in the following section. Therefore, adjusting the nozzle diameter and fluid extrusion flux accordingly promotes overall stability.

4.2.2 *Influence of printing speed*

Altering the printing speed is an effective way to enhance the construction speed, however, an excessive high printing speed can add uncertainties to the printing process [41]. Figure 9a indicates that

Fig. 7 Geometrical profile of one printed layer as influenced by the speed ratio S_R: **a** layer height and **b** layer width
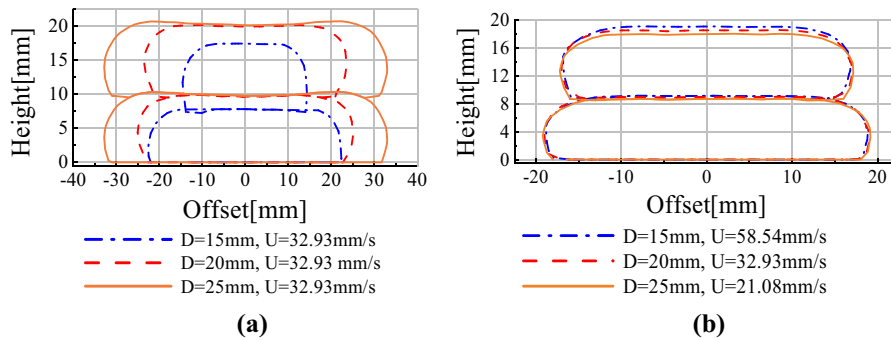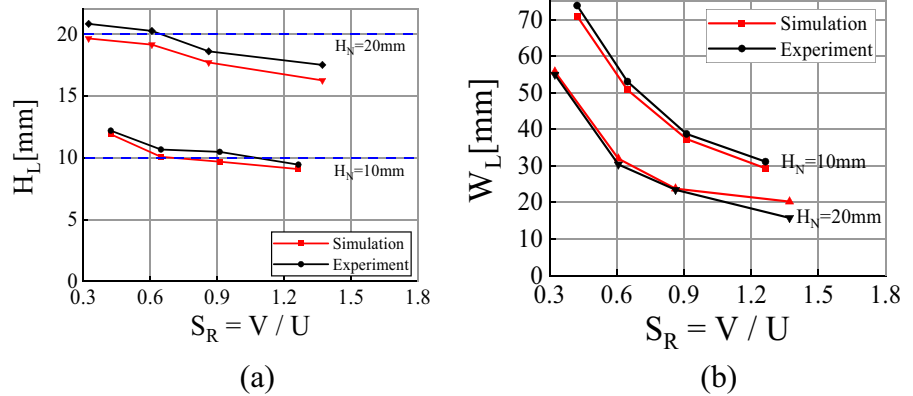
Fig. 8 The influence of nozzle diameter on the cross-sectional shape of two printed layers, **a** only changing the nozzle diameter, while other conditions remain the same ($V = 30$ mm/s, $H_N = 10$ mm), and **b** adapting fluid extrusion flux accordingly when changing the nozzle diameter ($V = 30$ mm/s, $H_N = 10$ mm)

Fig. 9 The influence of printing speed on the cross-sectional shape of two printed layers, **a** only changing the printing speed, while other conditions remain the same ($D = 20$ mm, $H_N = 10$ mm), and **b** adapting fluid extrusion flux accordingly when changing the printing speed ($D = 20$ mm, $H_N = 10$ mm)
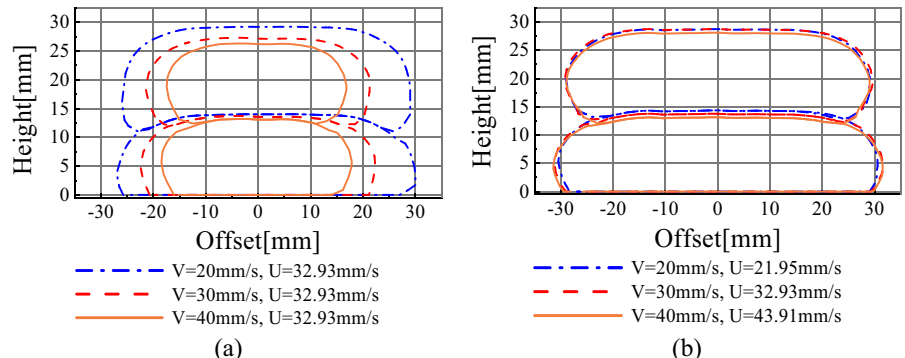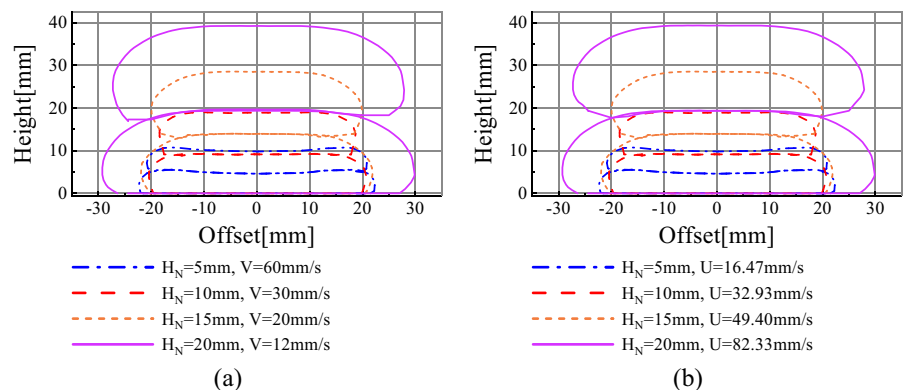
when solely modifying the printing speed (from 20 to 40 mm/s) with other factors being constant ($D = 20$ mm, $H_N = 10$ mm), the width of the printed object decreases correspondingly due to the reduced amount of material, resulting in a circular cross-section of the printed layers. This decreases the interlayer contact area, thereby increasing the possibility of geometric defects [42, 43].

If the flow rate is scaled while changing the printing speed, it can keep each layer of the printed body almost the same, ensuring the layer contact area, as shown in Fig. 9b. However, a faster speed and larger extrusion flow rate may increase local instantaneous extrusion stress, leading to greater vertical deformation, which will be further explained. Consequently, the material undergoes lateral deformation, posing a greater risk to the overall stability [16]. Therefore, altering the printing speed results in a higher risk for overall stability, whether only changing the speed or matching the corresponding working conditions. Therefore, adjusting the printing speed to match other factors is not recommended.

4.2.3 Influence of nozzle height

The effect of the nozzle height on the cross-sectional geometry is shown in Fig. 10. Different nozzle heights were compared, including 5, 10, 15, and 20 mm. Previous studies indicated that changing the nozzle height can also alter the deformation and stress distribution of each layer [44, 45]. Therefore, matching other processes, such as the printing speed or the extrusion flux, with the print height to obtain a better-printed layer and ensure proper layer stacking is required.

Two approaches, including adjusting the printing speed (from 12–60 mm/s) and the extrusion flux (from 16.47–82.33 mm/s), were adopted in the study. Other parameters such as the nozzle diameter (20 mm) were kept the same. As indicated in Fig. 10, although adjusting the printing speed or the extrusion flux can meet stability requirements, the effect on the plastic yielding remains complicated, which will be discussed further in Sect. 4.3.3.

### 4.3 Plastic yielding analysis

4.3.1 Influence of yield stress difference

Stacking the second layer applies two main components of force on the bottom layer: the self-weight of the top layer and the transient local squeezing stress of the printing nozzle. The plastic yielding region appears when the stress exceeds the yield stress of the extruded material. For the numerical analysis, the yield stress of the bottom layer material is denoted as $\tau_{0,1}$, the yield stress of the second layer material is denoted as $\tau_{0,2}$.

Figure 11a exhibits the plastic yielding region during extrusion. By assessing the volume of the material that reaches the yield stress in different cases, we can obtain a valid indicator of the likelihood of potential plastic yielding. The yield stress of the top layer is set as 405.7 Pa. It can be observed from the figure that when the yield stress of the bottom layer material is greater than 1000 Pa, no plastic yielding region can be found in the bottom layer, indicating that it can withstand all the loads during the extrusion process. Nevertheless, in case the yield stress of the bottom layer is at the same level as the second

Fig. 10 The influence of changing the printing height on the cross-sectional geometry of two printed layers, **a** changing the printing speed to match the printing height ($D = 20$ mm, $U = 32.93$ mm/s), and **b** changing the material extrusion flux to match the printing height ($D = 20$ mm, $V = 30$ mm/s)

Fig. 11 The influence of yield stress on plastic yielding, **a** distribution of plastic yielded region, and **b** plastic yielded area in function of yield stress ($D = 20$ mm, $V = 30$ mm/s, $H_N = 10$ mm)

(a)   (b)
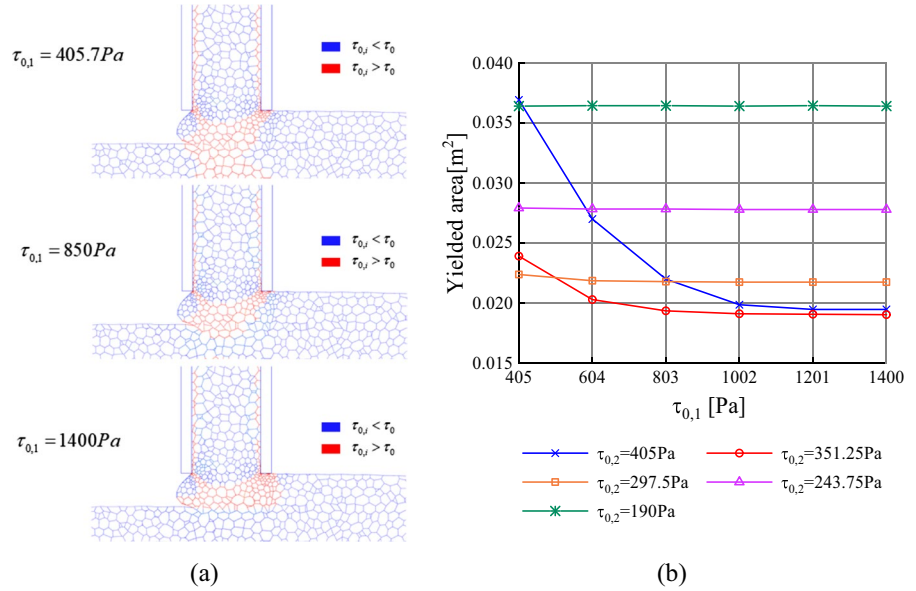
deposited layer, i.e. 405.7 Pa, a large yielded region can be observed.

The volume of plastic yielding in both layers is illustrated in Fig. 11b when the yield stress of the top and bottom layers changes. It can be observed that the volume of material reaching plastic yielding remains approximately constant when the yield stress of the bottom layer is large enough. This is because the bottom layer no longer yields during the extrusion process as the yield stress of the bottom layer reaches 1400 Pa, allowing it to withstand the upper load fully. In this case, only the top layer yields near the extrusion nozzle. In addition, if the yield stress of the top layer is minor, the upper layer load may not be able to transfer to the bottom layer. Therefore, as shown in the figure, when the yield stress of the cover layer is less than 297.5 Pa, it has a minimal effect on the bottom layer.

4.3.2 Influence of nozzle diameter

Figure 12a shows the distribution of plastic yielding inside the extruded layers with two representative nozzle diameters (20 and 25 mm). It is observed that

Fig. 12 The influence of nozzle diameter on the plastic yielding, **a** the distribution of plastic yielding, and **b** yielded area in function of nozzle diameter ($V = 30$ mm/s, $H_N = 10$ mm)

(a)   (b)
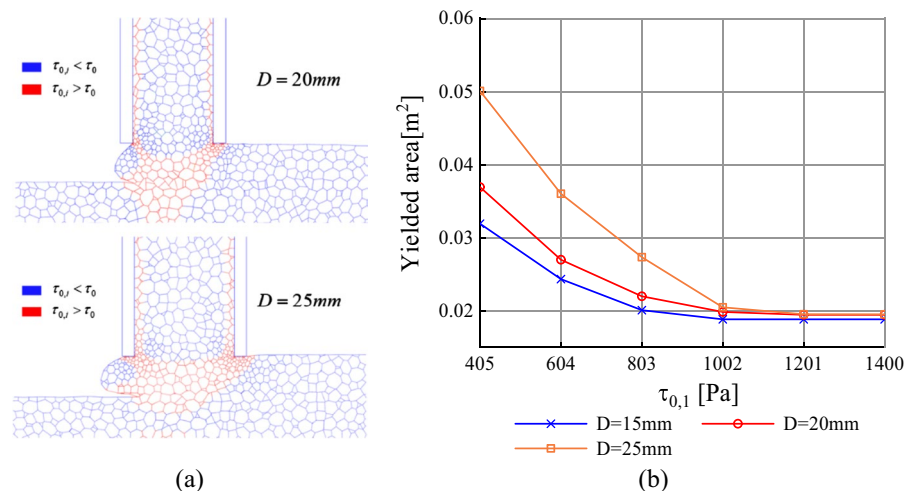
a smaller print nozzle diameter results in a smaller influenced region, causing stress concentration. In contrast, a larger print nozzle diameter results in a larger affected region and more dispersed stress. As discussed earlier, when the stress exceeds the yield stress, the material yields and undergoes plastic deformation. Figure 12b shows the yielded volume when printing nozzles with different diameters are used. The normalized yielded volume for printing nozzles with larger diameters is more than that using a smaller diameter. For example, for the extruded material with the yield stress of 405 Pa, when the nozzle diameter increases from 15 to 25 mm, the normalized yielded volume is raised from 0.032 to 0.05 m^2.

4.3.3 Influence of nozzle height

As can be seen in Fig. 13a, by changing the nozzle height, it is clear that the strain rate distribution inside the extruded material has changed. When the nozzle height is low, the printing direction of travel creates a large protrusion area with areas of stress concentration, resulting in two peak areas of stress concentration directly below the nozzle and at the protrusion part, leading to more severe material shear and a larger load on the bottom layer. This stress can penetrate the second layer and reach the bottom layer. In the case of adopting higher nozzle heights, less plastic yielding region is observed in the bottom layer.

This situation is also reflected in the pattern of volume change of the material reaching the yield stress obtained by varying the print height, as shown in Fig. 13b.

4.3.4 Influence of printing speed

The impact of increasing the printing speed on the yielded volume of extruded material is investigated in this section. As the material extrusion flux adjusts to the printing speed, there is a proportional rise in the material volume within a localized range, along with a corresponding increase in interaction between the current overlay and the underlying layer. When the top layer attains a yield stress of 190 Pa, there is no impact on the bottom layer, which is demonstrated in Fig. 14a, b. In addition, as illustrated in Fig. 14c, a decrease in printing speed from 40 to 30 mm/s leads to a lower yielded volume, while there is no distinct difference between the yielded volume when comparing a printing speed of 20 mm/s and 30 mm/s.

5 Conclusions

This paper discusses the plastic yielding resulting from various process parameters of 3D printable materials with multiple layers. The one-layer model is extended to two layers using a user-defined function

Fig. 13 The influence of nozzle height on plastic yielding, **a** strain rate distribution with different nozzle heights of 5, 10, and 15 mm, and **b** yielded area in function of the yield stress with different nozzle heights of 5, 10, and 15 mm ($D = 20$ mm, $V = 30$ mm/s)
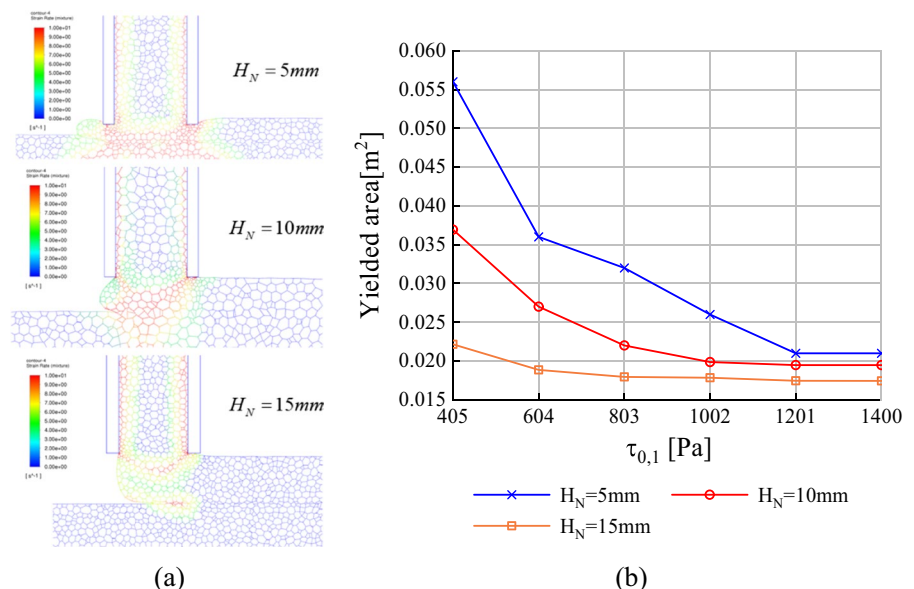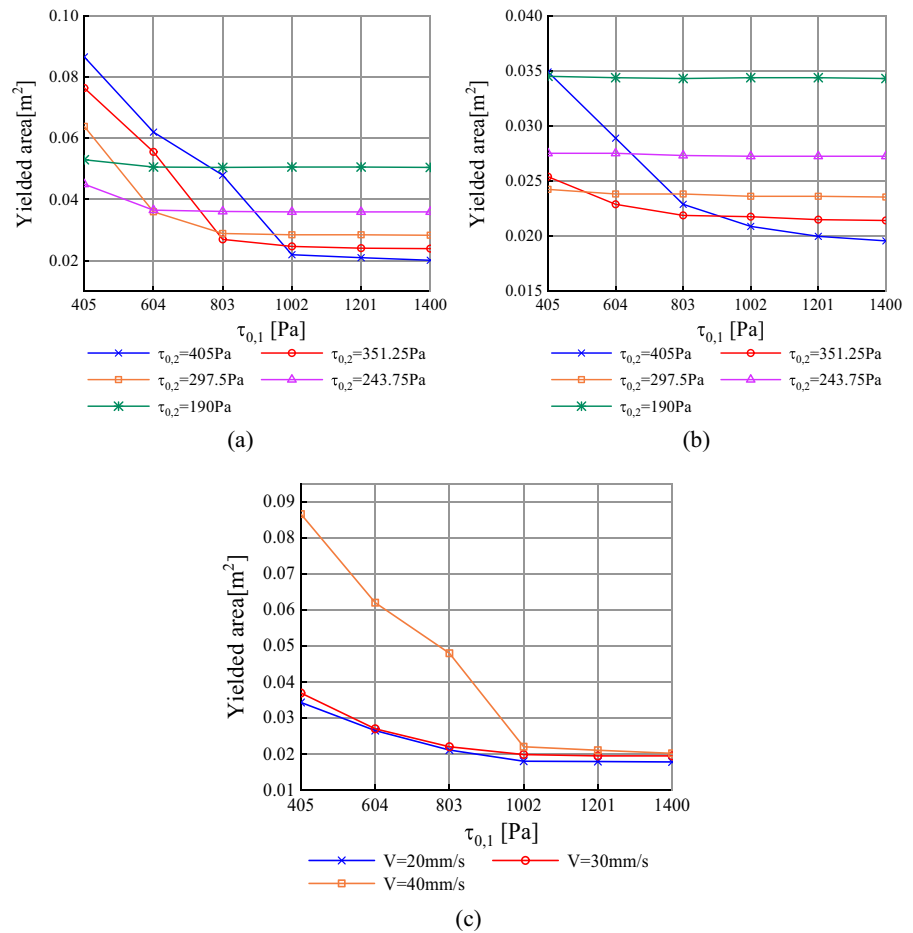
(a)   (b)

Fig. 14 Yielded area in function of the yield stress of the bottom layer, **a** different yield stresses of top layer with constant printing speed of 40 mm/s, **b** different yield stresses of top layer with constant printing speed of 20 mm/s, and **c** a constant yield stress of top layer with different printing speeds of 20, 30, and 40 mm/s ($D=20$ mm, $H_N=10$ mm)

loaded with source terms. Geometrical profiles of the extruded layers are compared and the volume of plastic yielding is also analyzed as influenced by the printing process parameters and material properties.

The virtual prints' cross-sectional geometry exhibits qualitative agreement with the physical prints, thereby validating the CFD modeling approach and the effectiveness of utilizing the Herschel Bulkley constitutive law to characterize the fresh material. Nevertheless, to further improve the model, the time-dependent behavior of the material, e.g. structural build-up, can be considered during the deposition of 3D printable concrete.

The printing parameters, as well as the yield stress of the material, remarkably influence the cross-sectional geometry. To maintain stability, randomly changing the printing speed is not advisable, but if the printing height must be altered, scaling the extrusion flow rate to match can yield a better printing quality.

Using smaller printing speeds can significantly reduce the volume of plastic yielded region and changing the nozzle diameter has a considerable effect on the strain rate distribution of the extruded top layer. Still, it is limited to the overall plastic yielding.

The current model has demonstrated the feasibility of simulating two-layer deposition, while extending the model to more layers with more complex shapes is challenging due to high computational cost. New strategies to reduce computational cost are desired. Adopting a multi-scale model might be a sound solution for more complex calculations.

References

1. Khoshnevis B (2004) Automated construction by contour crafting: related robotics and information technologies. Automat Constr 13(1):5–19. https://doi.org/10.1016/j.autcon.2003.08.012

2. Khoshnevis B, Hwang D et al (2006) Mega-scale fabrication by contour crafting. Int J Ind Syst Eng 1(3):301–320. https://doi.org/10.1504/IJISE.2006.009791

3. De Schutter G, Lesage K et al (2018) Vision of 3D printing with concrete: technical, economic and environmental potentials. Cem Concr Res 112:25–36. https://doi.org/10.1016/j.cemconres.2018.06.001

4. Lowke D, Dini E et al (2018) Particle-bed 3D printing in concrete construction: possibilities and challenges. Cem Concr Res 112:50–65. https://doi.org/10.1016/j.cemconres.2018.05.018

5. Buswell RA, da Silva WRL et al (2020) A process classification framework for defining and describing digital fabrication with concrete. Cem Concr Res 134:106068. https://doi.org/10.1016/j.cemconres.2020.106068

6. Chen Y, Chaves Figueiredo S et al (2020) Improving printability of limestone-calcined clay-based cementitious materials by using viscosity-modifying admixture. Cem Concr Res 132:106040. https://doi.org/10.1016/j.cemconres.2020.106040

7. Schwartz J (2018) Graphic statics and their potential for digital design and fabrication with concrete. Cem Concr Res 112:122–135. https://doi.org/10.1016/j.cemconres.2018.06.015

8. Zhang X, Li M et al (2018) Large-scale 3D printing by a team of mobile robots. Automat Constr 95:98–106. https://doi.org/10.1016/j.autcon.2018.08.004

9. Jacquet Y, Perrot A, Picandet V (2021) Assessment of asymmetrical rheological behavior of cementitious material for 3D printing application. Cem Concr Res 140:106305. https://doi.org/10.1016/j.cemconres.2020.106305

10. Mohan MK, Rahul AV et al (2021) Early age hydration, rheology and pumping characteristics of CSA cement-based 3D printable concrete. Constr Build Mater 275:122136. https://doi.org/10.1016/j.conbuildmat.2020.122136

11. Suiker ASJ, Wolfs RJM et al (2020) Elastic buckling and plastic collapse during 3D concrete printing. Cem Concr Res 135:106016. https://doi.org/10.1016/j.cemconres.2020.106016

12. Suiker ASJ (2022) Effect of accelerated curing and layer deformations on structural failure during extrusion-based 3D printing. Cem Concr Res 151:106586. https://doi.org/10.1016/j.cemconres.2021.106586

13. Vantyghem G, Ooms T, De Corte W (2021) VoxelPrint: a Grasshopper plug-in for voxel-based numerical simulation of concrete printing. Automat Constr 122:103469. https://doi.org/10.1016/j.autcon.2020.103469

14. Suiker ASJ (2018) Mechanical performance of wall structures in 3D printing processes: theory, design tools and experiments. Int J Mech Sci 137:145–170. https://doi.org/10.1016/j.ijmecsci.2018.01.010

15. Dinkgreve M, Paredes J et al (2016) On different ways of measuring "the" yield stress. J Nonnewton Fluid Mech 238:233–241. https://doi.org/10.1016/j.jnnfm.2016.11.001

16. Tao Y, Ren Q et al (2022) Shape stability of 3D printable concrete with river and manufactured sand characterized by squeeze flow. Cem Concr Comps 133:104674. https://doi.org/10.1016/j.cemconcomp.2022.104674

17. Meeten G (2002) Constant-force squeeze flow of soft solids. Rheol Acta 41(6):557–566. https://doi.org/10.1007/s00397-002-0241-3

18. Engmann J, Servais C, Burbidge AS (2005) Squeeze flow theory and applications to rheometry: a review. J Nonnewton Fluid Mech 132(1):1–27. https://doi.org/10.1016/j.jnnfm.2005.08.007

19. Wolfs RJM, Bos FP, Salet TAM (2018) Early age mechanical behaviour of 3D printed concrete: numerical modelling and experimental testing. Cem Concr Res 106:103–116. https://doi.org/10.1016/j.cemconres.2018.02.001

20. Wolfs RJM, Bos FP, Salet TAM (2018) Correlation between destructive compression tests and non-destructive ultrasonic measurements on early age 3D printed concrete. Constr Build Mater 181:447–454. https://doi.org/10.1016/j.conbuildmat.2018.06.060

21. Pott U, Stephan D (2021) Penetration test as a fast method to determine yield stress and structural build-up for 3D printing of cementitious materials. Cem Concr Comps 121:104066. https://doi.org/10.1016/j.cemconcomp.2021.104066

22. Ducoulombier N, Mesnil R et al (2021) The "Slugstest" for extrusion-based additive manufacturing: protocol, analysis and practical limits. Cem Concr Comps 121:104074. https://doi.org/10.1016/j.cemconcomp.2021.104074

23. Roussel N, Spangenberg J et al (2020) Numerical simulations of concrete processing: from standard formative casting to additive manufacturing. Cem Concr Res 135:106075. https://doi.org/10.1016/j.cemconres.2020.106075

24. Perrot A, Pierre A et al (2021) From analytical methods to numerical simulations: a process engineering toolbox for 3D concrete printing. Cem Concr Comps 122:104164. https://doi.org/10.1016/j.cemconcomp.2021.104164

25. Ramyar E, Cusatis G (2022) Discrete fresh concrete model for simulation of ordinary, self-consolidating, and printable concrete flow. J Eng Mech 148(2):04021142. https://doi.org/10.1061/(ASCE)EM.1943-7889.0002059

26. Remond S, Pizette P (2014) A DEM hard-core soft-shell model for the simulation of concrete flow. Cem Concr Res 58:169–178. https://doi.org/10.1016/j.cemconres.2014.01.022

27. Chang Z, Zhang H et al (2022) Numerical simulation of elastic buckling in 3D concrete printing using the lattice model with geometric nonlinearity. Automat Constr 142:104485. https://doi.org/10.1016/j.autcon.2022.104485

28. Hanada T, Kuroda K, Takahashi K (2016) CFD geometrical optimization to improve mixing performance of axial mixer. Chem Eng Sci 144:144–152. https://doi.org/10.1016/j.ces.2016.01.029

29. Jiang S, He Z et al (2022) Numerical simulation research on suction process of concrete pumping system based on CFD method. Powder Technol 409:117787. https://doi.org/10.1016/j.powtec.2022.117787

30. Comminal R, Leal da Silva WR et al (2020) Modelling of 3D concrete printing based on computational fluid dynamics. Cem Concr Res 138:106256. https://doi.org/10.1016/j.cemconres.2020.106256

31. Spangenberg J, LealdaSilva WR et al (2021) Numerical simulation of multi-layer 3D concrete printing. RILEM Tech Lett 6:119–123. https://doi.org/10.21809/rilemtechlett.2021.142

32. Mollah MT, Comminal R et al (2021) Stability and deformations of deposited layers in material extrusion additive manufacturing. Addit Manuf 46:102193. https://doi.org/10.1016/j.addma.2021.102193

33. Mollah MT, Comminal R et al (2023) Computational analysis of yield stress buildup and stability of deposited layers in material extrusion additive manufacturing. Addit Manuf 71:103605. https://doi.org/10.1016/j.addma.2023.103605

34. Serdeczny MP, Comminal R et al (2018) Experimental validation of a numerical model for the strand shape in material extrusion additive manufacturing. Addit Manuf 24:145–153. https://doi.org/10.1016/j.addma.2018.09.022

35. Yuan Q, Li Z et al (2019) A feasible method for measuring the buildability of fresh 3D printing mortar. Constr Build Mater 227:116600. https://doi.org/10.1016/j.conbuildmat.2019.07.326

36. El Cheikh K, Rémond S et al (2017) Numerical and experimental studies of aggregate blocking in mortar extrusion. Constr Build Mater 145:452–463. https://doi.org/10.1016/j.conbuildmat.2017.04.032

37. Reinold J, Nerella VN et al (2022) Extrusion process simulation and layer shape prediction during 3D-concrete-printing using the particle finite element method. Automat Constr 136:104173. https://doi.org/10.1016/j.autcon.2022.104173

38. Mohan MK, Rahul AV et al (2021) Extrusion-based concrete 3D printing from a material perspective: a state-of-the-art review. Cem Concr Comps 115:103855. https://doi.org/10.1016/j.cemconcomp.2020.103855

39. van den Heever M, du Plessis A et al (2022) Evaluating the effects of porosity on the mechanical properties of extrusion-based 3D printed concrete. Cem Concr Res 153:106695. https://doi.org/10.1016/j.cemconres.2021.106695

40. Liu H, Liu C et al (2022) Hardened properties of 3D printed concrete with recycled coarse aggregate. Cem Concr Res 159:106868. https://doi.org/10.1016/j.cemconres.2022.106868

41. Panda B, Tan MJ (2018) Experimental study on mix proportion and fresh properties of fly ash based geopolymer for 3D concrete printing. Ceram Int 44(9):10258–10265. https://doi.org/10.1016/j.ceramint.2018.03.031

42. Lao W, Li M, Tjahjowidodo T (2021) Variable-geometry nozzle for surface quality enhancement in 3D concrete printing. Addit Manuf 37:101638. https://doi.org/10.1016/j.addma.2020.101638

43. Liu Z, Li M et al (2020) Rotation nozzle and numerical simulation of mass distribution at corners in 3D cementitious material printing. Addit Manuf 34:101190. https://doi.org/10.1016/j.addma.2020.101190

44. Ji G, Xiao J et al (2022) Effects of extrusion parameters on properties of 3D printing concrete with coarse aggregates. Constr Build Mater 325:126740. https://doi.org/10.1016/j.conbuildmat.2022.126740

45. Kruger J, Zeranka S, van Zijl G (2019) 3D concrete printing: a lower bound analytical model for buildability performance quantification. Automat Constr 106:102904. https://doi.org/10.1016/j.autcon.2019.102904